APPLICATION OF FIRST ORDER UNIMOLECULAR RATE KINETICS TO INTERSTITIAL LASER PHOTOCOAGULATION

APPLICATION OF FIRST ORDER UNIMOLECULAR RATE KINETICS TO INTERSTITIAL LASER PHOTOCOAGULATION

by

TAMIE LYNN POEPPING

A Thesis

Submitted to the School of Graduate Studies

in Partial Fulfillment of the Requirements

for the Degree

Master of Science

McMaster University

MASTER OF SCIENCE (1996) McMaster University
(Medical Physics) Hamilton, Ontario

TITLE: Application of First Order Unimolecular Rate Kinetics to Interstitial Laser Photocoagulation.

AUTHOR: Tamie L. Poepping, B.Sc. (University of Alberta)

SUPERVISOR: Dr. Douglas R. Wyman

NUMBER OF PAGES: x, 57

ABSTRACT

An investigation of the temperature response and corresponding lesion growth resulting from *in vivo* interstitial laser photocoagulation was performed in order to test the applicability of Arrhenius theory. The irradiations were performed *in vivo* in rabbit muscle for various exposures at 1.0W using an 805 nm diode laser source coupled to an optical fibre with a pre-charred tip, thereby forcing it to function as a point heat source. Temperature responses were measured using a five-microthermocouple array along a range of radial distances from the point heat source. Each temperature profile was fitted with a curve predicted by the Weinbaum-Jiji bioheat transfer equation. The lesions were resected 48 hours after irradiation and the boundary of thermal damage resulting in necrosis was determined histologically. Numerical integration of the Arrhenius integral using temperature-time data at the lesion boundary produced corresponding activation energy and pre-exponential factor pairs (E_a , α) consistent with reported values for various other endpoints and tissue types. As well, theoretical predictions of the lesion growth from Arrhenius theory agreed well with experimental results. However, the thermal parameters, which are generally assumed to be constant when solving the bioheat transfer equation, were found to vary with radial distance from the source, presumably due to a dependence on temperature.

ACKNOWLEDGEMENTS

First off, I would like to thank my supervisor, Dr. Doug Wyman, for his guidance and encouragement throughout this project. I am also very grateful to Drs. Tom Chow and Claude Nahmias of my supervisory committee for their help and input, Dr. Otto Sanchez-Sweatman for his expertise on pathology and willingness to help at any time, Dr. Joe Hayward for all of his assistance, and Jeremy Gill for his computer wizardry. My sincere appreciation to all of the staff at the McMaster University Central Animal Facility for their hard work, especially Janis MacDonald for her help with the surgeries.

I would also like to thank my friends for all of their support especially Deidre Batchelar and Deboleena Roy for their advice and inspiration, and Sherry Spiller for her everlasting patience and encouragement.

Most importantly, I owe everything to my parents and family for their incredible love, support, and encouragement -- thank you.

TABLE OF CONTENTS

LIST OF FIGURES

LIST OF TABLES

NOMENCLATURE

A	Conventional pre-exponential factor ($A=\alpha*T$) (s^{-1})
a_0, a_1	Fit parameters of temperature response over time
b_1, b_2	Fit parameters for BHTE thermal parameters over radius
c	Specific heat (J/g/K)
D	Denatured state of molecule
E_a	Activation energy (kJ/mol)
h	Plank's constant (6.63×10^{-34} J·s)
k, k_1, k_{-1}, k_2	Reaction rates (s^{-1})
L_{th}	Thermal diffusion length (mm)
N, [N]	Native state molecule and corresponding molar concentration
N*, [N*]	Activated state of N and corresponding molar concentration
N_A	Avogadro's number (6.022×10^{23} mol^{-1})
P	Power delivered per unit volume (W/mm^3)
P_{total}	Total power delivered (W)
R	Gas constant (8.314 J/mol/K)
R_d^2	Coefficient of determination
r	Radius or radial coordinate (mm)
T	Temperature (°C)
T_{amb}	Ambient temperature (°C)
t	Time (s)
X	Thermal diffusivity (mm^2/s)
α	Pre-exponential factor ($s^{-1}K^{-1}$)
ΔS^*	Entropy of activation (J/mol/K)
κ_{eff}	Effective thermal conductivity (W/mm/K)
ρ	Density (g/mm^3)
ρc	Volumetric heat capacity, $\rho*c$ ($J/mm^3/K$)
Ω	Omega, damage parameter

CHAPTER 1

INTRODUCTION

1.1 INTERSTITIAL LASER PHOTOCOAGULATION

Interstitial laser photocoagulation (ILP) is a minimally invasive, experimental form of cancer therapy. It involves directing laser energy into a target volume through one or more implanted optical fibres and depositing sufficient energy to destroy the tissue through thermal coagulation. Its application is suited to destroying localized, unresectable tumors which is especially important within areas such as the brain, liver, or head and neck.

1.2 LASER SOURCE RATIONALE

The original concept of using laser light to induce thermal coagulation stemmed from several possible advantages in its application. First, the versatility of optical fibres enables them to be used endoscopically in order to reach sites non-invasively or to be inserted interstitially directly into a target volume. Second, the optical energy of the laser beam diffuses through the tissue before being absorbed and thus forms a distributed heat source. It was believed that maximizing optical diffusion would maximize volumes of damage and hence the continuous 1064 nm Nd:YAG laser was

initially preferred because of its maximal optical penetration in soft tissues (Svaasand *et al.*, 1985). However, further studies then revealed that significantly larger lesions could be produced with a point heat source (Wyman and Whelan, 1992) or less penetrating (ie. more strongly absorbed) wavelengths (Amin *et al.*, 1993). Both groups also found that larger lesions could be obtained by pre-charring the bare tip prior to irradiation and thereby forcing the point optical source to function as a point heat source.

The formation of char or carbonization during irradiations has both advantages and disadvantages. Carbonization produces possibly dangerous fragments as well as CO and CO_2 gases. The high temperatures associated with charring also result in water vaporization. For irradiations in liver, the production of gases and vapors in the form of microbubbles is actually necessary for monitoring the lesion using ultrasound. However, the possibility of the microbubbles coalescing suggests the risk of air embolisms which is of paramount concern for irradiations performed in the brain. Hence the continuous 1064 nm Nd:YAG laser appears to redeem itself as the optimal wavelength for use in brain due to the importance of avoiding these risks associated with high temperatures and charring. For other irradiation sites, the choice of wavelength and decision to pre-char the tip or not remains an issue open to debate.

1.3 THERMAL DAMAGE TO TISSUE

Thermal damage to biological material has been studied for many years. There are basically two problems to be faced in predicting the extent of thermal damage in

heated tissues. The first, is to predict the spatial and temporal variations in the temperature response of the surrounding tissue using mathematical/computer modelling. The second, is to determine what changes, physical and chemical, result from the temperature increases and then predict which of these changes are lethal. The true extent of thermal damage can be assessed histologically to confirm the predictions.

1.3.1 Predicting the Temperature Response of Irradiated Tissue

Predictions of the temperature distribution in the tissue over space and time are based on the bioheat transfer equation as discussed in section 2.2. A comparison and contrast of the various new bioheat transfer models is given by Arkin *et al.* (1994) including the Weinbaum-Jiji (W-J) bioheat transfer model (Weinbaum and Jiji, 1985) which will be used here. Some of the critiques of this model are also reviewed in Arkin *et al.* (1994).

1.3.2 Biological Response of Irradiated Tissue

1.3.2.1 Mechanisms of Laser-Tissue Interactions

Laser-tissue interactions can be divided into three categories: photochemical, photomechanical, and photothermal (Boulnois, 1986). Photochemical effects are produced by introducing special compounds which catalyze or induce damaging chemical reactions when selectively triggered. Photomechanical effects (photodisruption, photofragmentation) are the result of short, high peak power laser

pulses which result in rapid heating and expansion. The sudden expansion induces mechanical-acoustic shockwaves that disrupt cells or fragment tissue. Finally, photothermal effects result from the heating of tissue as light energy is absorbed leading to thermal injury such as coagulation or hyperthermia.

1.3.2.2 Identifying Zones of Thermal Damage

Thermal damage effects can be further divided into three categories corresponding to different thermodynamic processes and temperature regions (Pearce, 1990). At lower temperatures (40-100+°C), various damage processes, such as denaturation, are more probable as temperature increases and the damage accumulates with increasing exposure duration. For temperatures above 100°C, damage is dominated by water-vaporization effects such as extracellular vacuole formation and rupture (popcorn effect). Once the water is completely evaporated, extremely high temperatures (300-1000s °C) are reached in the remaining desiccated tissue with the onset of tissue ablation including combustion, molecular dissociation, plasma formation, carmelization, and carbonization.

The lower temperature effects can be further discriminated as either lethal or nonlethal thermal injury (Thomsen, 1991, Pearce and Thomsen, 1995). Nonlethal injury such as ruptured cellular membranes, distorted or swollen organelles (mitochondria, endoplasmic reticulum), and inactivation of enzymes may be reversible allowing the cell to recover over time. These effects are difficult to detect immediately after irradiation, although possible with enzyme histochemistry and

transmission electron microscopy. However, delayed effects secondary to the nonlethal injury such as hyperemia (vascular dilatation and congestion), and intracellular and tissue edema (abnormal accumulation of fluid) are good indicators of nonlethal damage and easily identified histologically.

Lethal injury occurs when the thermal damage is so severe that the repair mechanisms can not cope or the repair tools (DNA and/or RNA transcription enzymes) themselves are destroyed (Pearce and Thomsen, 1995). The full extent of *in vivo* thermal damage to tissue can only be determined approximately 24-72 hours post-irradiation when the cell death is manifested by necrosis. Necrosis is the natural degradation process of the dead cells and is easily identified by standard light microscopy.

1.3.2.3 Definition of Thermal Coagulation

In biological materials, a rise in temperature can result in the breakage of hydrogen and other van der Waals bonds that stabilize the conformation of molecules. Since biochemical reactions generally require a sort of lock-and-key fit, a loss of structural conformation ultimately results in a loss of function. These changes in the physical and physiological properties of a protein are termed denaturation. The global denaturation of structural proteins in the cells and tissues is a process known as coagulation. Thermal coagulation is immediately visible to the eye as a blanching or whitening of the tissue and is an indicator of immediate lethal thermal effect but not a good indicator of the outermost boundary of lethal effect.

1.3.3 Predicting the Accumulation of Thermal Damage

Many of the low temperature damage processes have been successfully modelled by first order unimolecular rate kinetics as discussed in section 2.3. In this model, thermal damage is defined as the time integral of the reaction rate, which is the net rate of change of the native or undamaged molecular species. For the model to be useful, a damage process, such as cell death or protein denaturation, must be coupled to an identifiable histopathological end-point such as tissue necrosis, loss of birefringence, or visual whitening/blanching.

1.4 SCOPE OF THIS PROJECT

The goal of this study is to investigate the long term growth of ILP thermal lesions. The first objective is to determine if growth is asymptotic or if significantly larger lesions can be produced with exposures beyond the conventional clinical exposures of 10 to 15 minutes. Secondly, the observed growth characteristics are to be reconciled with a mathematical model for thermal lesion growth. This model is based on Arrhenius theory whereby thermal coagulation and/or necrosis are quantified according to first order unimolecular rate kinetics.

CHAPTER 2

THEORY

2.1 INTRODUCTION

The mathematical modelling of interstitial laser photocoagulation is considered here in two parts. First, the temperature distribution is described by the bioheat transfer equation. Second, the tissue damage model is derived from the theory of rate processes.

2.2 HEAT DISTRIBUTION IN TISSUE

The theoretical distribution of heat within tissue is derived from the bioheat transfer equation (BHTE). It is a conservation of energy equation that balances the rate of energy storage with the rate of heat transfer and energy deposition. The BHTE includes the effects of heat transfer due to thermal conduction, convective heat transfer via blood perfusion, and thermal storage capacity. The original form first introduced by Pennes (1948) was modified by Weinbaum and Jiji (1985) to include the convective thermal effects of blood flow as an enhancement in the thermal conductivity. The resulting Weinbaum-Jiji (W-J) bioheat transfer equation is:

$$\rho c \frac{\partial T}{\partial t} = \nabla\cdot(\kappa_{eff}\nabla T(r,t)) + P(r,t) \qquad (2.1)$$

The enhanced thermal conductivity is known as the effective thermal conductivity, κ_{eff} (W/mm/K). Density, ρ (g/mm3), specific heat, c (J/g/K), and κ_{eff} are all tissue dependent parameters varying with the content of water, proteins, and fat or other nonaqueous ingredients (Takata *et al.*, 1974, Cooper and Trezek, 1971). The power source term, P(r,t), is the power deposited per unit volume. It should also be noted that contributions from metabolic heat generation have been ignored here but can be added as a fourth term or included in the source term.

The W-J bioheat equation has been the subject of much attention and examination, as discussed in Charney *et al.* (1990) and Arkin *et al.* (1994), with regards to its proper use. From these two sources it can be summarized that the W-J equation is only strictly applicable to muscle tissue (with low blood perfusion) that contains blood vessels with diameters less than 0.2 mm or to tissues in general provided the ratio between thermal equilibration length and actual vessel length is less than 0.3.

If κ_{eff} is assumed to be constant, it can be taken outside of the derivative and the BHTE solved analytically (Wyman and Whelan, 1994) using Green's function methods. Solving for the transient temperature increase above ambient, T (K), in equation 2.1 for a point heat source in an infinite, homogeneous medium produces the temperature distribution:

$$T(r,t) = T_{amb} + \frac{P_{total}}{4\pi\kappa_{eff}\, r} \cdot erfc\left(\frac{r}{L_{th}(t)}\right) \qquad (2.2)$$

where r (mm) is radial distance from the source and $L_{th}(t)$ is the thermal diffusion length at time t given by $(4\kappa_{eff}\, t/\rho c)^{1/2}$. For a steady-state temperature increase ($\partial T/\partial t=0$), the complementary error function term, erfc, is eliminated from the above temperature distribution which becomes an inverse distance profile.

2.3 MODELLING OF THERMAL DAMAGE

2.3.1 Rate Process Kinetics

Reaction kinetics have been used (Arrhenius 1889, Henriques and Moritz 1947, Birngruber 1980) to model the rate processes of thermal damage. In a typical reaction, a native reactant must be thermally activated to overcome an energy barrier resulting in an intermediate state of higher free energy, as shown in figure 2.1. This energy of activation, E_a (J/mol), is acquired through collision with other molecules. The reaction scheme for a unimolecular process resulting from the collision of native state molecules, N, that are activated to an intermediate state, N*, before reaching the final denatured state, D is given by:

$$N + N \underset{\leftarrow k_{-a}}{\overset{\rightarrow k_a}{\rightleftharpoons}} N + N^{*} \qquad N^{*} \xrightarrow{k_d} D \tag{2.3}$$

where k_a, k_{-a}, and k_d are the reaction rates. The rate of disappearance of native state molecules is given by:

$$-\frac{d[N]}{dt} = k\,[N] \tag{2.4}$$

where the brackets indicate molar concentration. The overall reaction rate, k, here

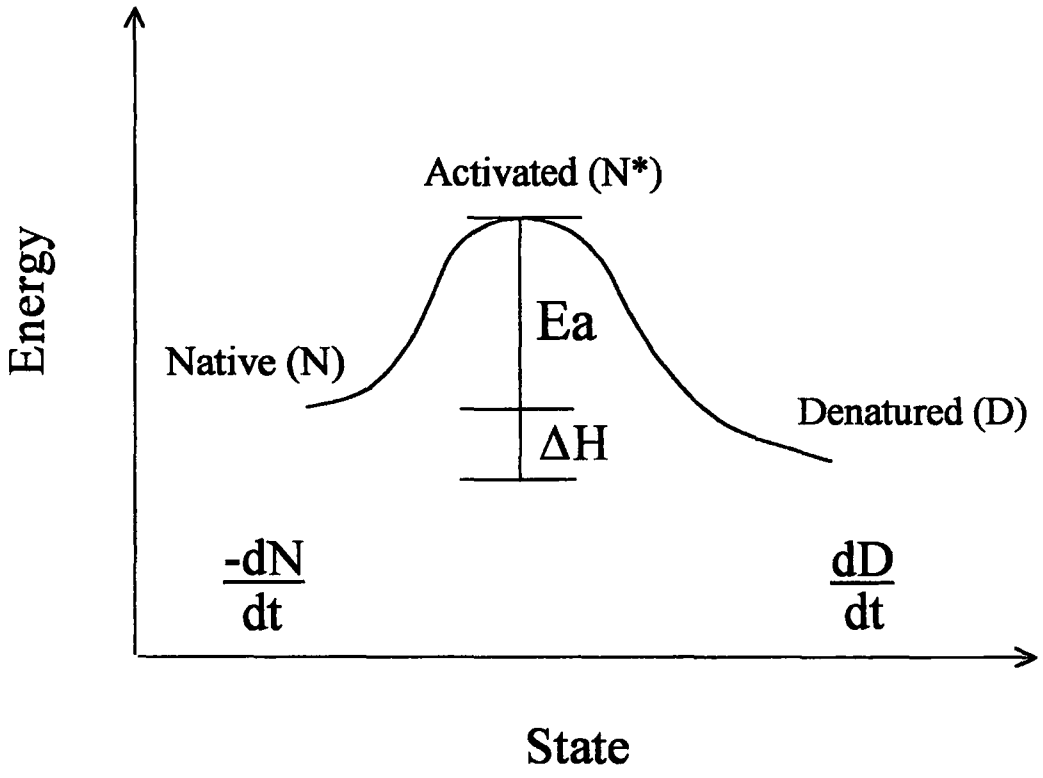

Figure 2.1: Reaction curve for the process of protein denaturation showing the variation in free energy as the reaction progresses from the native species to activated and denatured states.

has been shown (Birngruber 1980, Pearce and Thomsen 1995) to be $k_d k_a / k_{-a}$ in the limiting case that the remaining concentration of native state molecules is still large enough such that $k_{-a}[N] >> k_d$. In this case, equation 2.4 is a first-order rate process with the solution:

$$N(t) = N_0 \, e^{-\int_0^t k dt'} \tag{2.5}$$

where N_0 is the original concentration or number of native state molecules and N(t) is the amount remaining at some specified time.

2.3.2 Arrhenius Integral

The integral in equation 2.5 is known as Arrhenius' integral:

$$\Omega(t) = \int_0^t k dt' = \ln \frac{N_0}{N(t)} \tag{2.6}$$

where the parameter Ω quantifies the amount of thermal damage. The reaction rate calculated from statistical theory (Birngruber, 1980):

$$k = \frac{RT}{N_A h} \, e^{\frac{\Delta S^*}{R} - 1} \, e^{\frac{-E_a}{RT}} \tag{2.7}$$

can be substituted into equation 2.6 giving:

$$\Omega(t) = \int_0^t \frac{RT}{N_A h} e^{\frac{\Delta S^*}{R} \cdot 1} e^{\frac{-E_a}{RT}} dt' = \alpha \int_0^t T(r,t') e^{\frac{-E_a}{RT(r,t')}} dt' \quad (2.8)$$

In these equations, R is the universal gas constant, N_A is Avogadro's number, h is Planck's constant, ΔS^* is the entropy of activation (J/mol/K), and α is the pre-exponential factor (s^{-1} K^{-1}). This is a slightly modified form of the conventional Arrhenius integral where the T(r,t) term is approximated to be constant relative to the exponential term and hence included in the front factor outside of the integral. Equation 2.8 can only be solved numerically for transient temperature distributions such as equation 2.2.

CHAPTER 3

MATERIALS & METHODS

3.1 APPARATUS

3.1.1 Laser Source

An 805 nm diode laser system (Model LDP-4380C-6C, Laser Diode Inc., Edison, New Jersey) coupled to a 400 um optical fibre was used to deliver continuous-wave laser energy at 1.0 or 1.2 W. The optical power output was calibrated using an Ophir laser power meter (Model DG, Optikon, Waterloo, Ontario). The fibre jacket and cladding were stripped back 5 mm from the plane-cut tip to avoid melting. The end (~2 mm) of the bare tip was precharred, forcing it to function as a point heat source rather than a point optical source.

3.1.2 Temperature Measurements and Recording

Temperatures were measured using 0.009" (~230 um) diameter copper-constantan (type T) microthermocouples (Model IT-23, Physitemp Instruments Inc., Clifton, New Jersey). The individual wires of the thermocouples are encased in Teflon® PTFE with a Teflon PFA coating on the probe junction . The thermocouples are connected to the analog input of a data acquisition system (Labmate series 7000,

Scientific Instruments Inc., Nepean, Ontario) controlled by a 10 MHz AST Premium/286 microcomputer using modified Labmate software. Temperature measurements are saved to file upon completion of the run.

The control software allows selection of the number of thermocouple inputs, the time between temperature measurements, and the total number of temperature measurements. The minimum time between temperature measurements is limited however by the run time of the software and the total number of thermocouple inputs. Allowing for this, a five second time interval between temperature measurements was selected.

The accuracy of temperature measurements was tested using a water bath (15-100°C) and high precision Hg thermometer (0.1°C increments). The temperatures measured by the thermocouples were found to agree within ±0.5°C of those from the Hg thermometer. Slightly larger variations were observed *in vivo*, however temperatures still agreed within ±1°C.

A five-thermocouple array was built where the thermocouples were staggered lengthwise along the axis by 1 mm. The set of five were inserted into a plastic catheter such that the most distal 3 to 7 mm of the measuring end, for thermocouples #1 to #5 respectively, were left exposed to ensure better contact .

3.1.3 Delivery Template

Initial attempts to position the fine microthermocouples interstitially in tissue revealed very limited accuracy hence the thermocouples and fibre were arranged

between two slabs of tissue which were compressed slightly to simulate interstitial insertion. Observations of lesion size and temperatures from this modified set up were consistent with interstitial placement and hence suggest an acceptable modification.

In order to ensure consistently accurate placement of the thermocouple array relative to the optical fibre source, the array and fibre were arranged perpendicular to each other and fixed to a thin Lucite annulus as shown in figure 3.1(a). The annulus was 1 mm thick with an inner diameter of 3 cm and outer diameter of 5 cm. The template size was limited by the size of the irradiation site in the animal model. The thermocouples were originally fixed at 3, 4, 5, 6, and 7 mm from the fibre tip but were adjusted to 6, 7, 8, 9, and 10 mm to accommodate the larger 30 minute lesions.

3.2 EXPERIMENTAL PROCEDURE

3.2.1 Animal Model & Surgery

Irradiations were performed *in vivo* in rabbit muscle using healthy 2.0-3.5 kg female New Zealand White rabbits. Minor surgery allowed access to the rear leg muscles where the superficial fascia was opened and the semitendinous and semimembranous muscle groups were partially separated.

A pre-anesthesia mixture of 5 mg/kg of xylazine, 50 mg/kg of ketamine, and 1 mg/kg of acepromazine was injected intramuscularly. General anesthesia was then induced with 2-3% enflurane by volume in oxygen and maintained with 3-5% enflurane. Normal blood-oxygen levels were maintained by supplying oxygen at one

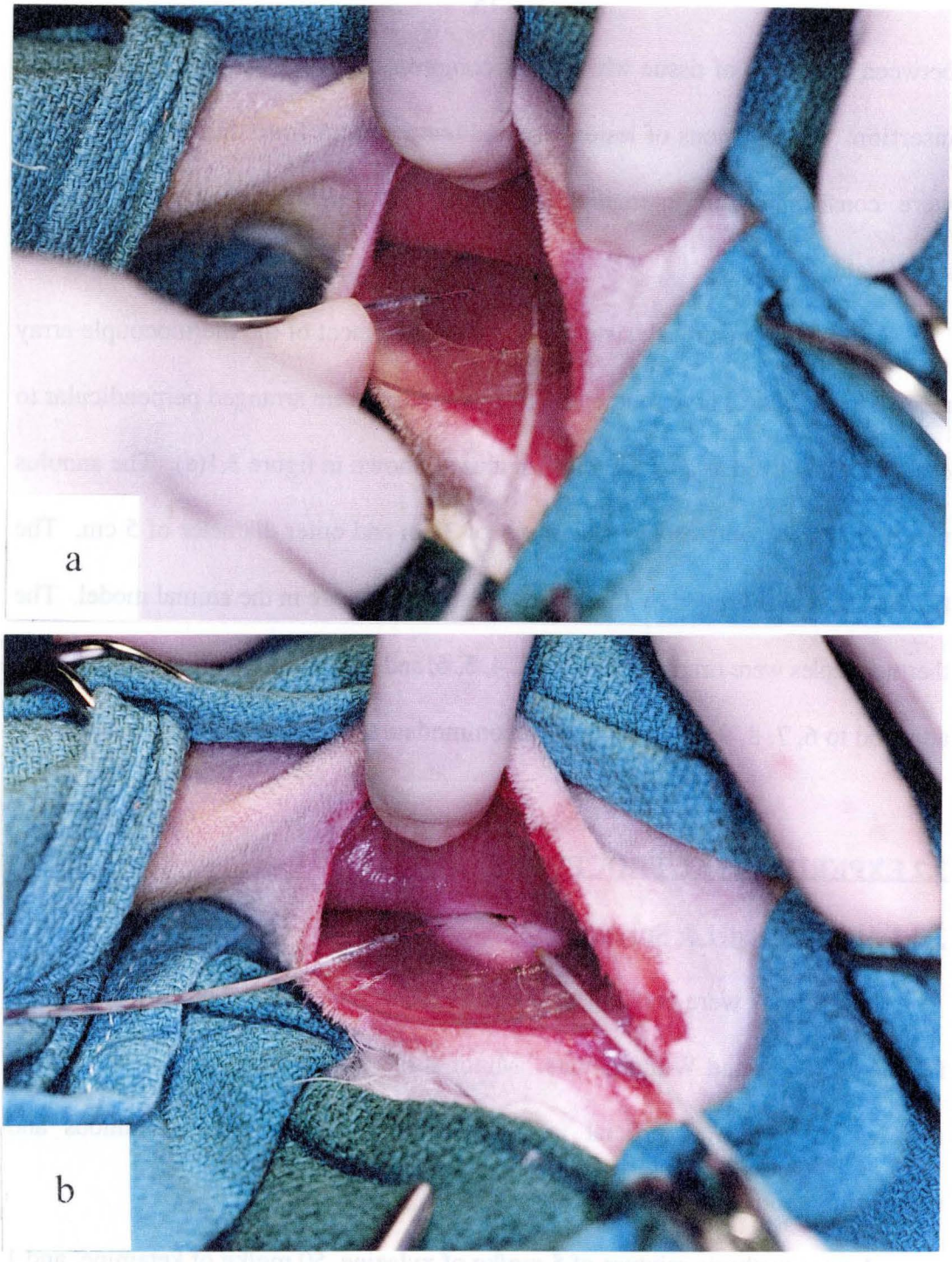

Figure 3.1: *In situ* placement of template with attached optical fibre and five-thermocouple array for an *in vivo* irradiation shown (a) pre-irradiation and (b) post irradiation.

litre per minute through a nose mask and the enflurane was mixed with the oxygen supply via a vaporizer. The pulse rate and blood-oxygen saturation level were monitored using a pulse-oximeter. Saline solution was administered by an intravenous drip through an artery in the ear to prevent dehydration. Body temperature was maintained during the surgery by placing a heating pad, on medium heat, under the anesthetized rabbit to prevent a drop in body temperature. An analgesic (buprenorphine, 0.01-0.05 mg/kg) was administered subcutaneously before recovery and every 8-12 hours thereafter.

3.2.2 Irradiation Protocol

The optical fibre tip was pre-charred using a small sample of blood that had been collected from the angiocatheter before inserting the intravenous line. The entire delivery template was then inserted between the semitendinous and semimembranous muscle groups as shown in figure 3.1(b). The template was placed such that the direction of the optical fibre was parallel to the muscle fibres for reasons discussed in section 4.2.1. During irradiation, the muscles were moderately compressed to ensure good contact and simulation of interstitial insertion but not so heavily compressed so as to limit blood flow. Temperature measurements were acquired every five seconds throughout each irradiation, commencing and finishing at the same times as the irradiation.

Initially, a delivered power of 1.2 W was used. However the 30 minute thermal lesions were large enough to reach the inner edge of the annular template. Therefore

in order to reduce the overall size of the lesions and keep them well within the tissue-tissue interface region, the power was reduced to 1.0 W. Three 10 minute, three 20 minute, and five 30 minute irradiations were performed in total at 1.0 W. Generally, a longer irradiation in one leg was matched with a shorter irradiation in the other in order to reduce the total time under anesthesia for any one rabbit.

At the end of each irradiation, a second fibre was used to make small coagulation marks on the semimembranous muscle at a few points around the inner diameter of the template. These served as reference points of a known distance from the centre char. All lesion dimensions measured from the fixed samples or from the microscope slides could then be scaled to correct for shrinkage or stretching, due to preserving or processing techniques for example, and thereby obtain the proper *in vivo* dimensions. Due to the orientation of the surgical site, it was only possible to mark the semimembranous muscle and hence all lesion measurements were taken from this muscle section.

3.2.3 Sample Resection & Processing

Each animal was sacrificed 48 hours after irradiation and the lesions were photographed. Large portions of the upper and lower muscle groups containing the lesions were excised in order to maintain proper shape and size of the lesion. The resected samples were fixed in formalin for at least 24 hours before being prepared for histology. Only the larger, semimembranous muscle was used for lesion measurements since reference marks could not be made on the semitendinous muscle,

as mentioned earlier.

The semimembranous muscle section was cut (figure 3.2) across the source's centre point perpendicular to the optical and muscle fibre directions. From one of the half pieces, an approximately 2 mm transverse slice was taken from this centre cut and slides were prepared from the centre face. The second half piece was cut into two along the optical fibre track and perpendicular to the interface surface. From one of these quarter pieces, a 2 mm thick surface slice was taken. The slices were paraffin embedded and slides were prepared using each of an haematoxylin and eosin (H&E) stain and Masson's trichrome stain.

3.2.4 Histology

Microscope slides were examined using light microscopy and studied under the supervision of a collaborating pathologist. The necrosis boundary for each lesion was determined from the transverse section and the dimensions measured using the Vernier scale on the microscope under 10x magnification.

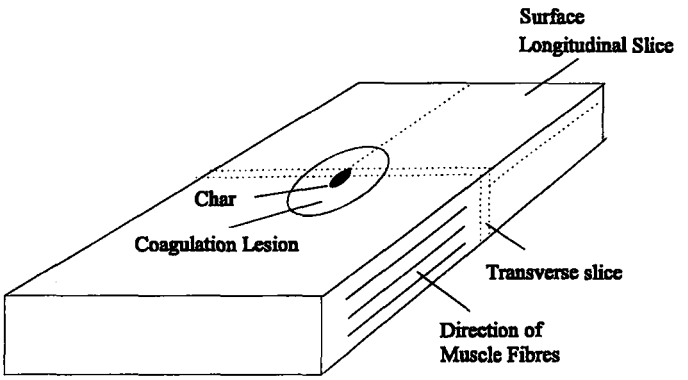

Figure 3.2: Schematic of slicing of extracted semimembranous muscle for histology sections.

CHAPTER 4

RESULTS & DISCUSSION

4.1 *IN VIVO* TEMPERATURE RESPONSE

4.1.1 Experimental Temperature Response

By recording the temperatures every five seconds throughout the irradiation, an adequately complete temperature response was acquired with a small random noise contribution. However, small jumps and spikes were occasionally seen to occur at identical times for the five thermocouples. This non-random noise contribution was attributed to small hand movements while holding the template in place and adding slight compression to ensure good contact between the two muscle groups. A typical temperature response for a 30 minute irradiation is shown in figure 4.1.

4.1.2 Temperature - Time History of Necrosis Boundary

Once the necrosis boundary had been determined histologically, the corresponding temperature profile was determined. This was done by linear interpolation, or extrapolation in a few instances, from the temperature profiles at the two nearest radii along the thermocouple array track. Figure 4.2 shows that a linear interpolation between radii is a reasonable approximation.

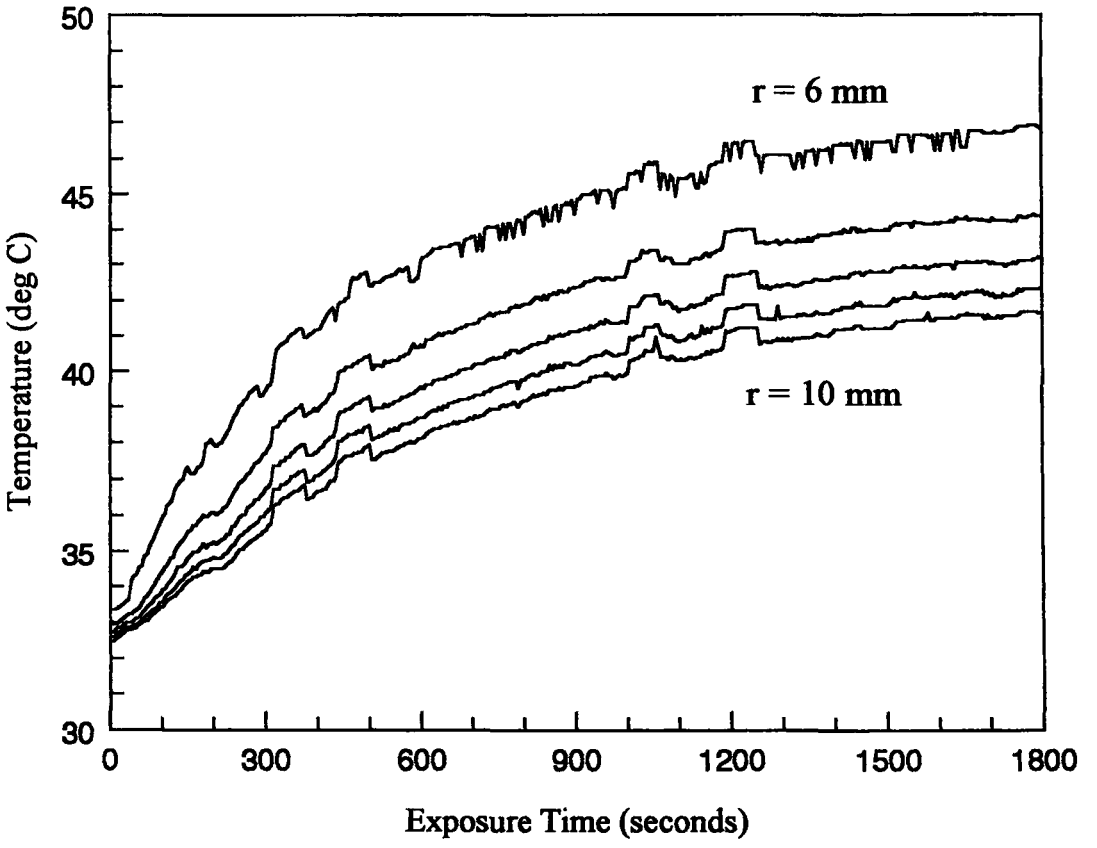

Figure 4.1: Recorded *in vivo* temperature response as a function of exposure for a typical 30 minute irradiation. Each profile represents the temperature response at a different radial distance from the source.

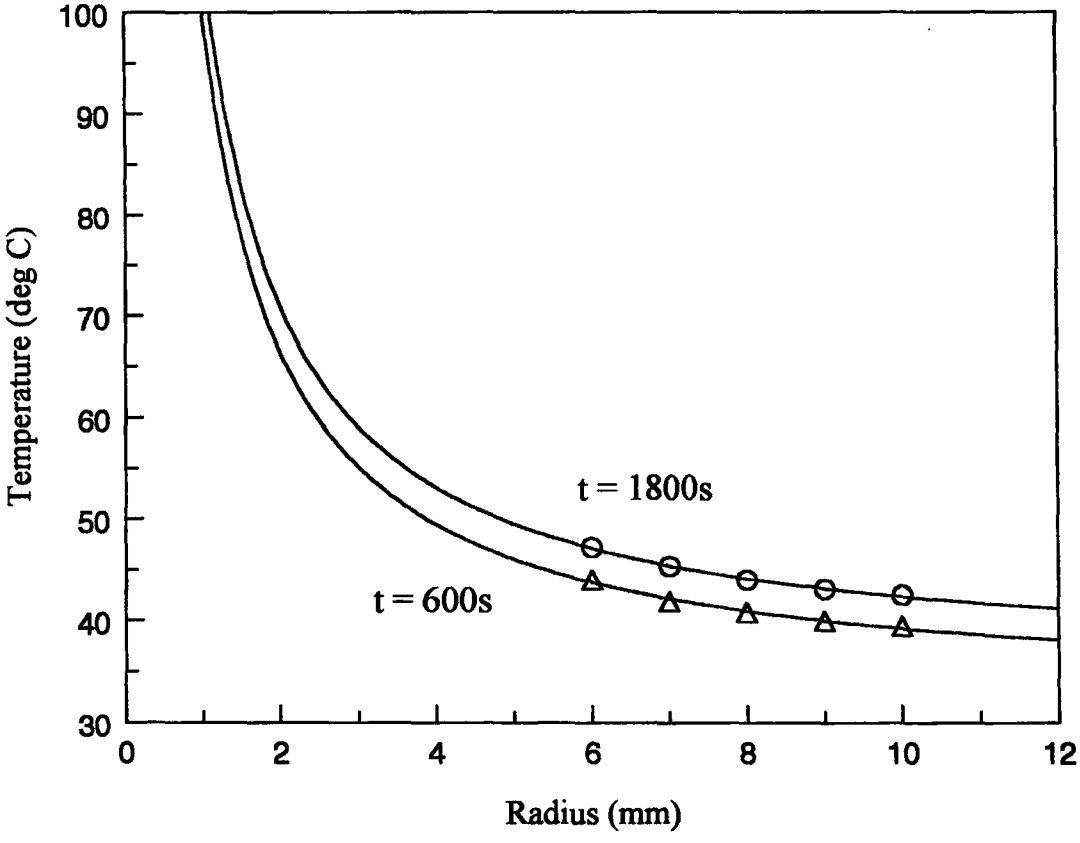

Figure 4.2: Temperature response as a function of the radial distance from the point heat source for a typical 30 minute irradiation. Data sets represent a snapshot in time at 600 seconds (triangles) and 1800 seconds (circles) from the start of the irradiation fitted to the theoretical model according to: $T=T_{amb}+(b_0/r)\text{erfc}(b_1 \cdot r)$. Uncertainty in each point is ±1 °C.

The Arrhenius integral (equation 2.8) was calculated from the temperature-time data by numerical integration using the trapezoid rule. This required selecting a suitable activation energy for calculating the integral. Reference values found in the literature varied from 128 kJ/mol (Pearce and Thomsen, 1995) to 783 kJ/mol (Weaver and Stoll, 1969) as shown in table 4.1. However, no references could be found for previous experimental work in skeletal muscle. Table 4.1 shows that several experiments have determined E_a to be around 300 kJ/mol, indicating this to be a reasonable energy to use when given no other argument for discrimination.

Numerical integration of the temperature-time data leads to a value for the ratio Ω/α. The pre-exponential factor, α, was then determined using the data corresponding to the necrosis boundary, where Ω is defined as one. The value of α was seen to vary slightly between the exposure groups. For 10, 20, and 30 minute irradiations, respectively, the average α was found to be $(4\pm3)\times10^{44}$, $(2\pm1)\times10^{44}$, and $(1.4\pm0.5)\times10^{44}$ $s^{-1}K^{-1}$. That is the values were slightly smaller for the longer exposures but all agreed within uncertainty. Not surprisingly, the variation was also dependent on the E_a used with larger variation observed for higher E_a values.

For completeness, the integration was also done for several other values of E_a as shown in table 4.2. Plotting the natural logarithm of the factor α versus the activation energy as in figure 4.3 shows the obvious correlation of the two. The solid line shows the linear fit to the experimental data (open circles) from table 4.2. Recall that the Arrhenius integral (equation 2.8) used here is a modified version of the

Activation Energy, E_a (kJ/mol)	Pre-Exponential Factor, A (s^{-1})	Tissue & Endpoint	Conditions	Source
128	3.12×10^{20}	Rabbit myocardium, in vitro, loss of birefringence		Pearce and Thomsen, 1995
258	(6.5×10^{38})*	Liver, visual whitening		Jacques *et al.*, 1991
293	1×10^{44}	Retina		Birngruber, 1985
297	(2.8×10^{46})*	Rat liver, delayed necrosis		Jacques *et al.*, 1991(data from Matthewson *et al.*, 1987)
306	1.6×10^{45}	Rat skin, birefringence		Pearce and Thomsen, 1993
327	1.8×10^{51}	Skin	$T \geq 323K$	Weaver and Stoll, 1969
339	4.11×10^{53}	Porcine skin, in vivo, purpura formation		Pearce and Thomsen, 1995
385	3.8×10^{57}	Egg white, whitening		Yang *et al.*, 1991
389	3.05×10^{56}	Egg yolk, whitening		Yang *et al.*, 1991
420	4.3×10^{64}	Retina	$316<T<323K$	Takata *et al.*, 1974
430	5.6×10^{63}	Human aorta		Pearce and Thomsen, 1993
628	3.1×10^{98}	Pig skin, in vivo		Henriques and Mortiz, 1947
628	3.1×10^{99}	Bovine retina		Welch and Polhamus, 1984
670	9.3×10^{104}	Retina	$T>323K$	Takata *et al.*, 1974
783	2.2×10^{124}	Skin	$317<T<323K$	Weaver and Stoll, 1969

*Calculated from ΔS values using $A=(RT/N_A h)\exp(\Delta S/R +1)$, T=330 K.

Table 4.1: Experimentally determined activation energies and corresponding pre-exponential factors.

Activation Energy, E_a (kJ/mol)	Pre-Exponential Factor, α (s^{-1} K^{-1})
100	$(1.1\pm0.2)\times10^{11}$
120	$(2.4\pm0.3)\times10^{14}$
200	$(4.8\pm0.7)\times10^{27}$
300	$(1.9\pm.3)\times10^{44}$
400	$(7\pm1)\times10^{60}$
420	$(1.4\pm0.3)\times10^{64}$
500	$(2.6\pm0.7)\times10^{77}$
600	$(9\pm3)\times10^{93}$
670	$(3.1\pm0.8)\times10^{105}$

Table 4.2: Experimentally determined pre-exponential factors and corresponding selected activation energies.

Data Set (P-E Factor)	Slope ($x10^{-3}$ mol/J)	Intercept	Goodness of fit (R_a^2 coefficient)
α	.3818±.0003	-(12.7±0.1)	.999
A/(330K)	.371±.006	-(12±3)	.997
A	.370±.005	-(5±3)	.998

Table 4.3: Linear fit parameters for natural log of pre-exponential (P-E) factor versus activation energy as in figure 4.3.

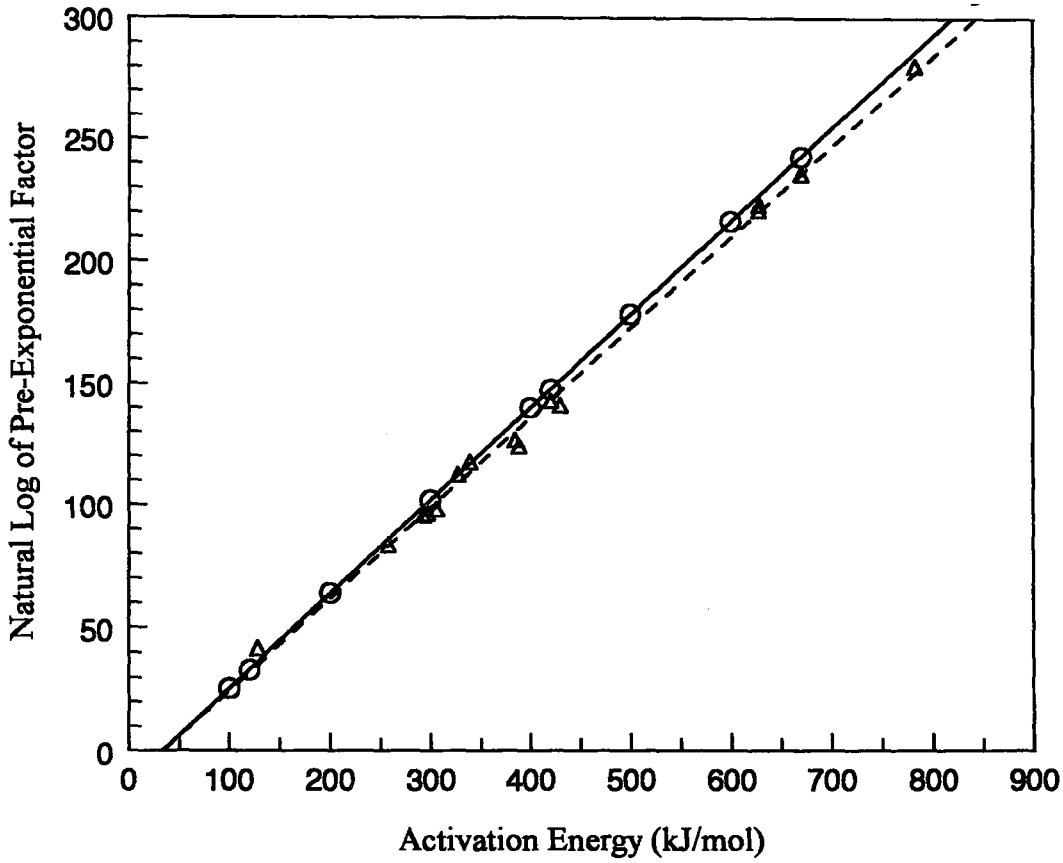

Figure 4.3: Natural logarithm of the pre-exponential factor, α, calculated using various E_a (open circles). Other reported (E_a , α) combinations (referenced in table 4.1) are plotted (open triangles) along with their corresponding fit (dashed line) where the approximation $\alpha \sim A/(330K)$ has been used.

conventional form where the conventional pre-exponential factor, denoted by A, is simply α*T. In the conventional form, T is assumed to be constant (~330 K) relative to the rapidly changing exponential term. Hence in order to be comparing similar factors, the natural logarithm of A/(330 K) was plotted (open triangles) along with its linear fit (dashed line) in figure 4.3. The fit parameters are given in table 4.3.

4.1.3 Fitting the Theoretical Model to the Experimental Temperature Response

For each measurement radius, the temperature-time profile was fit to the theoretical temperature distribution given in equation 2.2 according to the following two-parameter form of the equation:

$$T(r,t) = T_{amb} + a_0 \cdot erfc \frac{a_1}{\sqrt{t}} \qquad (4.1)$$

as shown in figure 4.4. The first temperature value recorded (at five seconds) for each profile was inserted into equation 4.1 as the ambient temperature, T_{amb}. The effective thermal conductivity was calculated from the first fit parameter, a_0, and the thermal diffusivity, X, which is given by ($\kappa_{eff}/\rho c$), was calculated from the second fit parameter, a_1. Using these two values, the product ρc, known as the volumetric heat capacity, was determined.

4.1.4 Variation in Effective Thermal Conductivity

Figure 4.5 shows the effective thermal conductivity as a function of radial

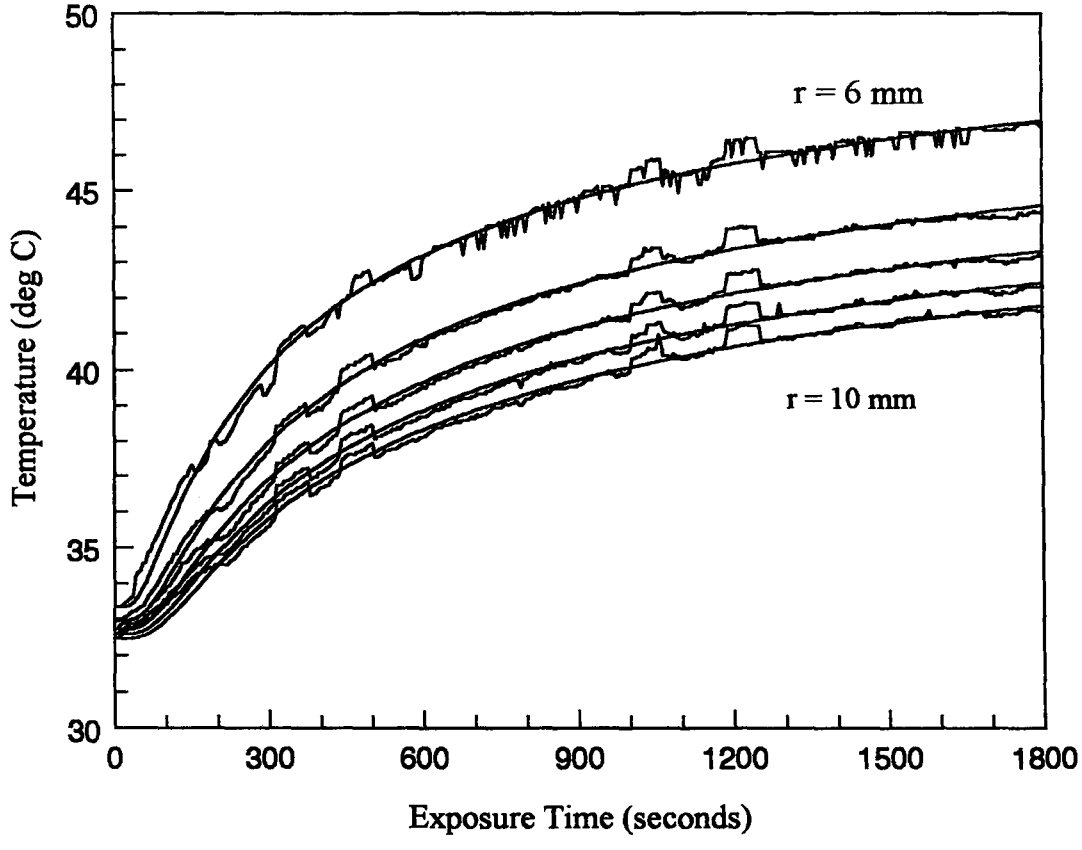

Figure 4.4: Theoretical temperature distribution model fitted to the experimental temperature response for a 30 minute irradiation. Each temperature-time profile, representing the response at a different radial distance from the source, was fitted to a two-parameter equation of the model.

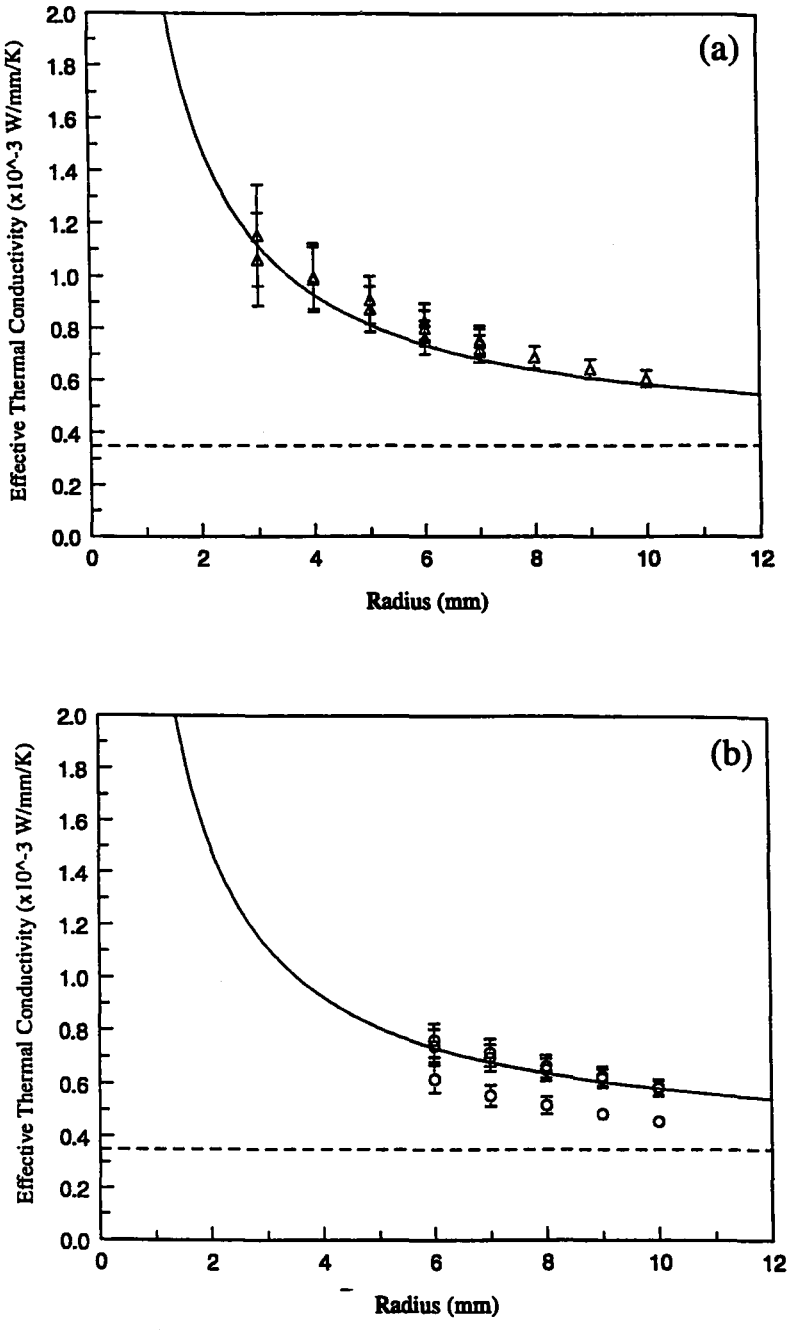

Figure 4.5: Dependence of experimental effective thermal conductivity on radial distance from the source for various exposures: (a) 10 minutes (triangles), (b) 20 minutes (circles), (c) 30 minutes (inverted triangles), and (d) threshold/lesion

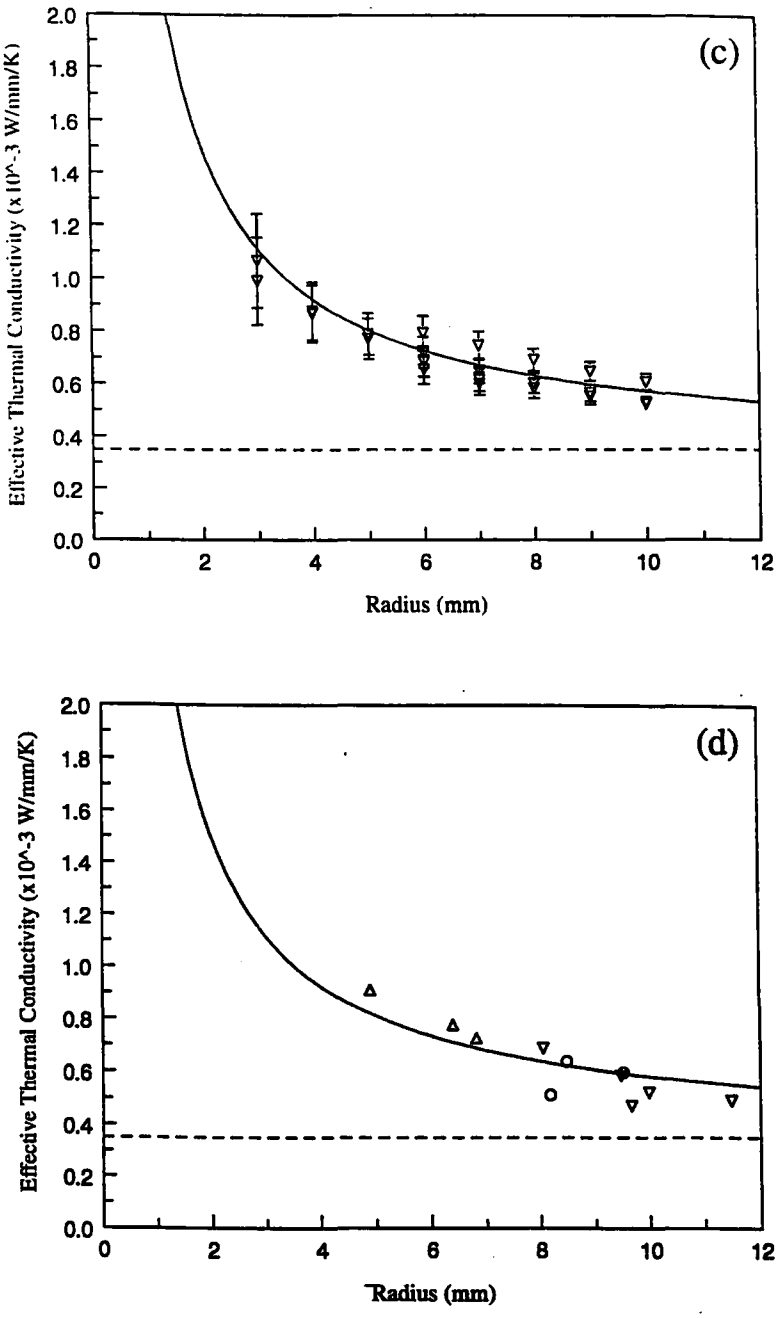

Figure 4.5(Continued): boundary values. The overall fit for the 10, 20, and 30 minute data combined is shown on each for comparison. The asymptote at $(0.35\pm0.02)\times10^{-3}$ W/mm/K, determined from the fit, is also shown.

distance from the point heat source. Typically, the thermal conductivity of tissue is in the range (0.3-0.5)x10^{-3} W/mm/K and for water is approximately 0.6x10^{-3} W/mm/K (Svaasand *et al.*, 1985). These nominal values, however, match the lower limits of what was observed and figure 4.5 indicates that these values correspond to radial distances well into the normal tissue and lower temperature regions. This inverse variation with radius, described in table 4.4, suggests that thermal conductivity increases with temperature which has also been demonstrated by Valvano and Chitsabesan (1987). Figure 4.5(d) shows the thermal conductivities derived from the lesion boundary temperature profiles and indicates that no conclusion can be made on how the conductivity varies with coagulation or damage. The variation seen again reflects the temperature dependence of κ_{eff} with higher conductivities observed with the higher temperature/shorter exposure irradiations and vice versa. It has been reported (Takata *et al.*, 1977) however that the conductivity varies directly with the water content. Hence it would be expected that the increasing conductivity will reach an upper limit at higher temperatures which contribute to the loss of water (ie. vaporization, 100+°C).

4.1.5 Variation in Thermal Diffusivity and Volumetric Heat Capacity

Figure 4.6 shows the variation of the derived thermal diffusivity with radial distance. The diffusivity ranged from 0.14 to 0.22 mm^2/s with an average of (0.188±0.002) mm^2/s for the 55 measurement points which is higher than the value for most tissues, 0.12 mm^2/s, reported by Svaasand (1985) or for water, 0.14 mm^2/s.

Parameter	Equation of Best Fit	b_1	b_2	R_d^2 Coefficient
Effective Thermal Conductivity	b_1+b_2/r	$(0.35\pm0.02)\times10^{-3}$	$(2.3\pm0.1)\times10^{-3}$	0.841
Thermal Diffusivity	b_1+b_2*r	0.148 ± 0.004	$(5.9\pm0.6)\times10^{-3}$	0.620
Volumetric Heat Capacity	b_1+b_2/r^2	0.0016	0.25 ± 0.01	0.801

Table 4.4: Summary of equations of best fit as a function of radius for the tissue-dependent thermal parameters.

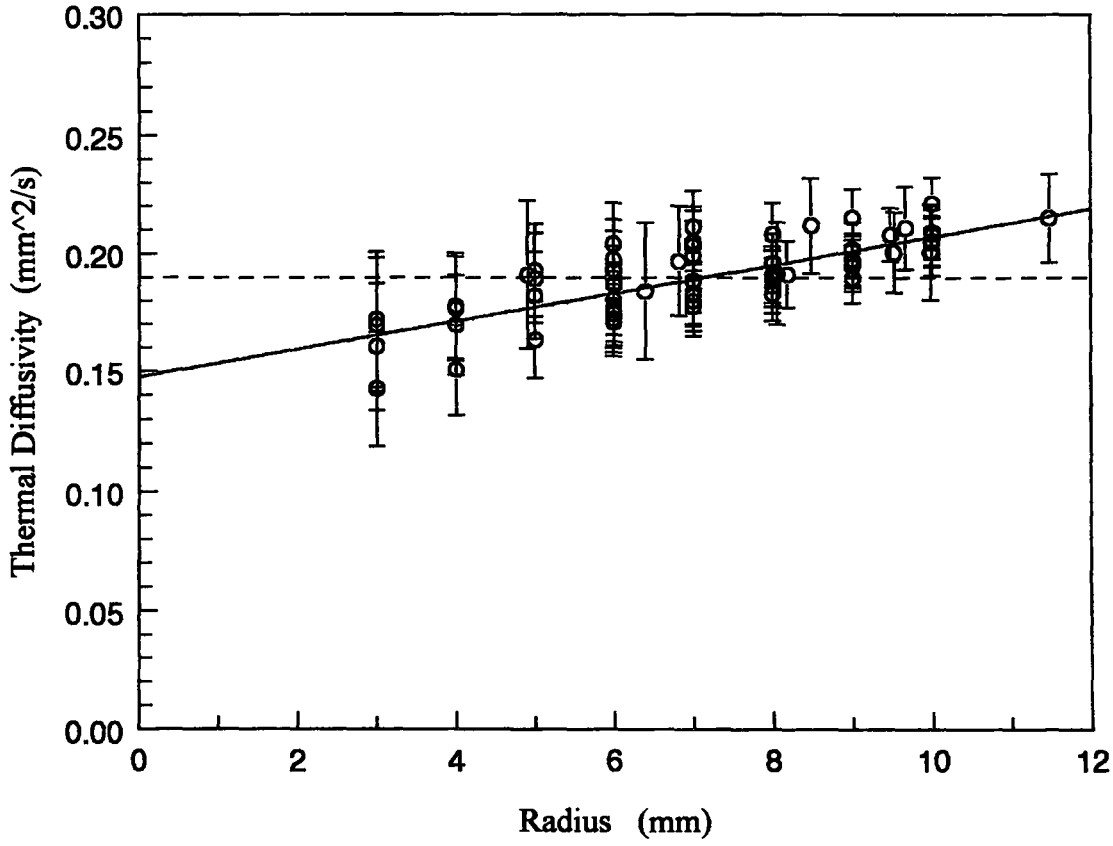

Figure 4.6: Variation in the thermal diffusivity with radial distance from the point heat source. The linear fit is shown by the solid line while the dashed horizontal line represents the average thermal diffusivity.

The data were fitted to the linear equation described in table 4.4 using Slide Write (©Advanced Graphics Software Inc., v. 3.0). The increase with radius, ie. decrease with temperature, is contrary to the observation of increasing diffusivity with temperature made by Valvano and Chitsabesan (1987). The trend observed here, however, simply indicates that the volumetric heat capacity, ρc, must vary more strongly with radius and hence temperature than the effective thermal conductivity. This is demonstrated in figure 4.7 where the volumetric heat capacity was best fitted as an inverse function of the radius squared. These fit parameters are also given in table 4.4. The observed values of ρc varied from approximately $4x10^{-3}$ J/mm^3/K to $40x10^{-3}$ J/mm^3/K which is considerably larger than the $4.2x10^{-3}$ J/mm^3/K reported for water.

4.2 EXPERIMENTAL LESION GROWTH

4.2.1 Constrictions in Irradiation Setup

Preliminary irradiations showed that although the whitened, coagulated area had circular symmetry, the resulting lesion including necrosis, edema, and inflammation was elongated along the length of the muscle fibres. Likely this is simply due to the leukocytes and fluids being able to preferentially seep along the interstitial area parallel to the fibres. As well, lesion growth is sometimes elongated along the optical fibre due to water vapor travelling back along the fibre. In order to avoid consistency problems due to this artifact of asymmetric growth in muscle, the template was always

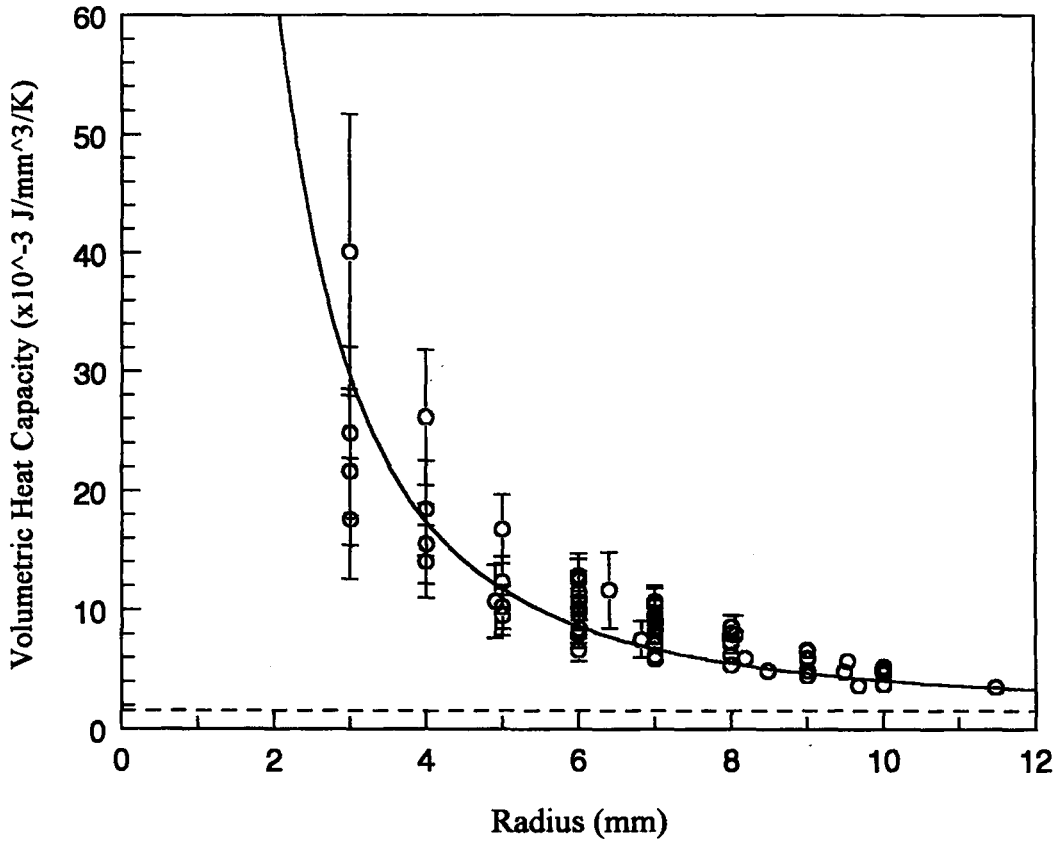

Figure 4.7: Variation of the volumetric heat capacity, ρc, with radial distance from the point heat source. The solid line represents the fit of ρc as a function of the inverse of radius squared. The dashed horizontal line shows the asymptote of this fit at 1.6×10^{-3} J/g/K.

positioned such that the muscle fibres were parallel to the optical fibre and perpendicular to the thermocouple array.

4.2.2 Determination of Necrotic Lesion Radius

4.2.2.1 Experimental Measurements

The lesion radius was measured along the thermocouple track. The radius on the opposite side of the lesion was also measured to assess symmetry and consistency, but only the coagulation radius along the thermocouple array track was included in the analyzed data. The necrosis radii for the eleven *in vivo* irradiations of varying exposure duration are shown in table 4.5 and figure 4.8 along with the average necrosis radius for each exposure group. Increasing the exposure length from 10 to 20 minutes extends the lesion radius by 2.7±0.7 mm or 45±13% while the increase from 20 to 30 minutes produces a 1.0±0.7 mm or 12±8%. The large uncertainties here are indicative of the sample or inter-experimental variation and not the incremental lesion growth. That is, if the size of a single lesion could be observed over time, the incremental growth would be more consistent than the actual lesion size. So a lesion of 4 mm radius after 10 minutes exposure will increase to approximately 7 mm and 8 mm after 20 and 30 minutes respectively just as one of 6 mm radius will similarly increase to approximately 9 mm and 10 mm.

Figure 4.8 provides evidence that thermal lesion growth is not necessarily asymptotic at 30 minutes, although the large uncertainties in lesion radii and variation between experiments renders a definite conclusion impossible.

EXPOSURE DURATION (minutes)	LESION LABEL	NECROSIS RADIUS (mm)	AVERAGE NECROSIS RADIUS* (mm)	SAMPLE STANDARD DEVIATION
10	θ-L	4.9±0.7	6.0±0.6	1.0
	ι-R	6.8±0.8		
	κ-L	6.4±0.9		
20	λ-R	8.5±0.8	8.7±0.4	0.7
	μ-L	8.2±0.6		
	ν-R	9.5±0.8		
30	θ-R	9.5±0.5	9.7±0.6	1.2
	ι-L	9.7±0.8		
	κ-R	8.1±0.9		
	λ-L	10±1		
	μ-R	11±2		

*Uncertainty given is standard error in the mean, $\sigma/\sqrt{N}$.

Table 4.5: Thermal lesion radii measured from 11 *in vivo* irradiations in rabbit muscle.

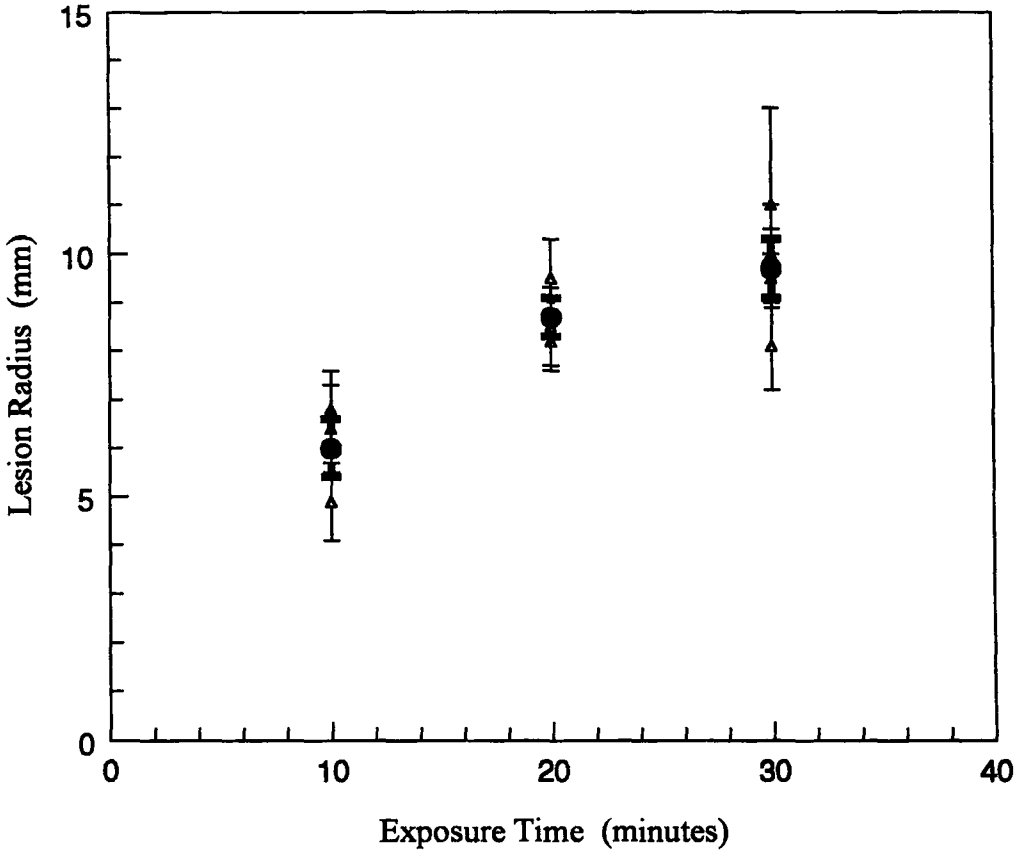

Figure 4.8: Radial growth of thermal lesions as a function of exposure duration for *in vivo* irradiations in rabbit muscle. Closed circles show the mean radius, including the standard error in the mean, observed for each exposure duration.

4.2.2.2 Theoretical Predictions

The difficulty in predicting thermal lesion size from transient temperature responses arises from not being able to analytically solve the Arrhenius integral (equation 2.8) for radial distance, r. For constant or steady-state temperatures, T(r), the integral reduces simply to:

$$\Omega(t) = \alpha\ t\ T(r)\ e^{\frac{-E_a}{RT(r)}} \tag{4.2}$$

where t is the total length of exposure. This equation can not be solved generally for r since it appears both outside and inside the exponent. A numerical solution can be obtained by iterating on the equation:

$$r = \frac{\frac{P_{total}}{4\pi\kappa_{eff}} R \ln(\frac{\alpha t T(r)}{\Omega(t)})}{E_a - T_{amb} R \ln(\frac{\alpha t T(r)}{\Omega(t)})} \tag{4.3}$$

where:

$$T(r) = -T_{amb} + \frac{P_{total}}{4\pi\kappa_{eff} r} \tag{4.4}$$

For transient temperature responses, T(r,t), (such as equation 2.2) the Arrhenius integral (equation 2.8) must be calculated by numerical integration for various (r,t) combinations. The lesion growth as a function of exposure time is determined by

finding each corresponding (r,t) pair resulting in Ω equal to one.

An IDL (Interactive Data Language, ©Research Systems Inc., v. 3.5.1) program was written (Appendix A) to numerically integrate equation 2.8 using an E_a of 300 kJ/mol and α of 1E44 and then determine the lesion radius as a function of exposure duration. This was repeated for several combinations of the tissue-dependent thermal parameters (κ_{eff}, ρc) as shown in figure 4.9. A reasonable fit to the experimental data was found for κ_{eff} and ρc equal to 0.6×10^{-3} W/mm/K and 3 J/mm^3/K respectively. The resulting curve is shown in figure 4.10 superimposed on the experimental data.

Assuming that the experimental data are well represented by the theoretical model of lesion growth for the thermal parameters shown, figure 4.10 then suggests that lesion growth is not asymptotic by 30 minutes. Although growth is most dramatic in the first 10 minutes, and less so thereafter, the plot indicates that larger lesions can be achieved with extended exposure durations.

4.3 CONSEQUENCES OF RADIAL/TEMPERATURE DEPENDENCE OF THERMAL PARAMETERS

As was shown in figures 4.5 and 4.7, a large range of κ_{eff} and ρc values were observed including values considerably higher than the usual ones found in the literature. The theoretical growth curves in figure 4.9 for varying thermal parameters show significantly reduced lesion size for larger thermal parameters. Curve 4 on figure 4.9 corresponding to 0.6×10^{-3} W/mm/K and 4.2 J/mm^3/K for κ_{eff} and ρc

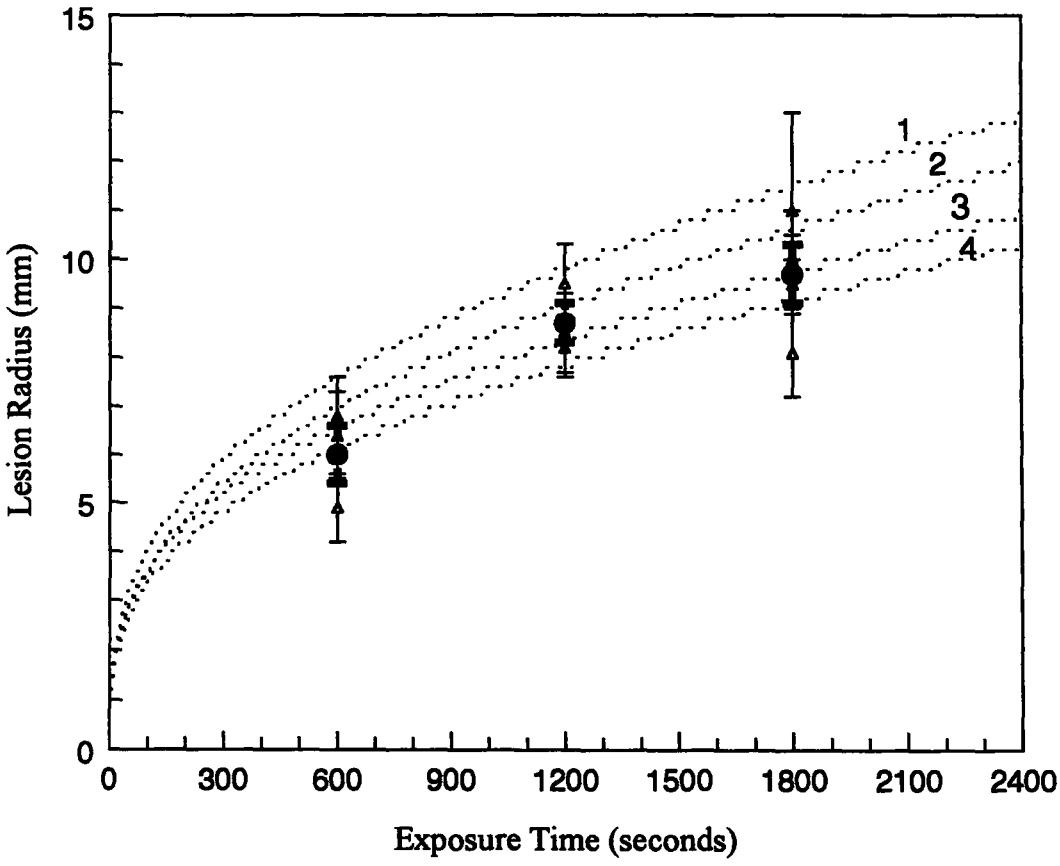

Figure 4.9: Lesion growth calculated numerically from the theoretical model compared to the experimental data (of figure 4.8). Curves 1 to 4 were determined using the following κ_{eff} and ρc values respectively: (*1*) 0.4×10^{-3} W/mm/K, 3 J/mm^3/K, (*2*) 0.4×10^{-3} W/mm/K, 4.2 J/mm^3/K, (*3*) 0.6×10^{-3} W/mm/K, 3 J/mm^3/K, (*4*) 0.6×10^{-3} W/mm/K, 4.2 J/mm^3/K.

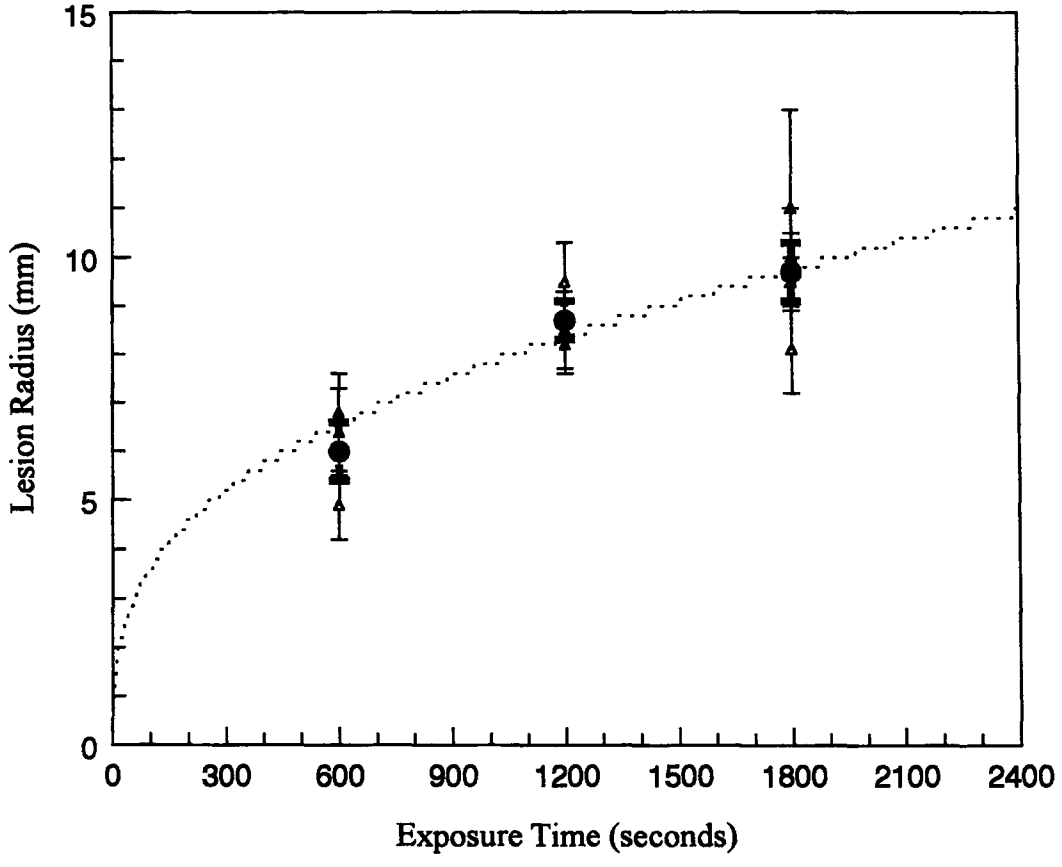

Figure 4.10: Theoretical lesion growth curve selected as the best fit to the experimental data. Theoretical curve was generated using E_a of 300 kJ/mol, α of 1E44, κ_{eff} of 0.6×10^{-3} W/mm/K, and ρc of 3 J/mm^3/K.

respectively represents maximal thermal parameters that will still provide a reasonable fit to the experimental lesion sizes. However, observed κ_{eff} and ρc values ranged well above these.

This trend of reduced lesion size with increasing thermal parameters would seem to indicate a negative feedback response. That is, initial lesion growth while thermal parameters are still low would follow curve 1, for example, and then essentially jump growth curves as the irradiation progressed and thermal parameters increased. In this case, lesion growth would very quickly become asymptotic due to the dramatic increases observed in the thermal parameters.

However, the spatial and temporal variations in the thermal parameters could also be advantageous for maintained lesion growth. The higher temperatures leading to increased conductivity and volumetric heat capacity are also associated with regions inside the necrosis boundary (ie. already damaged or killed cells). Increased conductivity in this inner region means that heat is conducted out towards the native tissue more quickly than if κ_{eff} were constant. Furthermore, the temperature response will be flattened hence the dangerously high temperatures near the centre are less likely to be reached or at least, to be reached less quickly. However, as mentioned earlier, the increasing conductivity and volumetric heat capacity will be capped once the temperatures are high enough to start reducing the water content of the tissue. At this point, thermal conduction out to the native tissue boundary will be slowed and lesion growth may become asymptotic.

4.4 VALIDITY OF THEORETICAL MODELS

4.4.1 Bioheat Transfer Equation

The predicted temperature distribution (equation 2.2) from the bioheat transfer equation (equation 2.1) fit very well to the experimental *in vivo* temperature responses. However, the thermal parameters determined from the fits were seen to increase with decreasing radial distance from the source, ie. increasing temperature. This contradicts the assumption of constant thermal parameters made in solving the bioheat transfer equation and indicates a need for including spatio-temporal variations in the thermal parameters when solving the equation.

4.4.2 Arrhenius Theory and First Order Unimolecular Rate Kinetics

In general, the results of these experiments were observed to be consistent with Arrhenius theory and therefore with first order unimolecular rate kinetics. First, the values of α calculated for each lesion boundary, using a given E_a , agreed within uncertainty despite different exposure lengths and differences in the temperature-time history. Figure 4.11 shows lesion boundary temperature responses for 10, 20, and 30 minute irradiations which result in similar values, $(2.5\pm0.5)\times10^{44}$, for α. As predicted from Arrhenius theory, higher temperatures were required with shorter exposures to produce the same damage.

Second, the correlation between E_a and the corresponding α calculated for each E_a value by numerical integration of the lesion boundary temperature-time data was

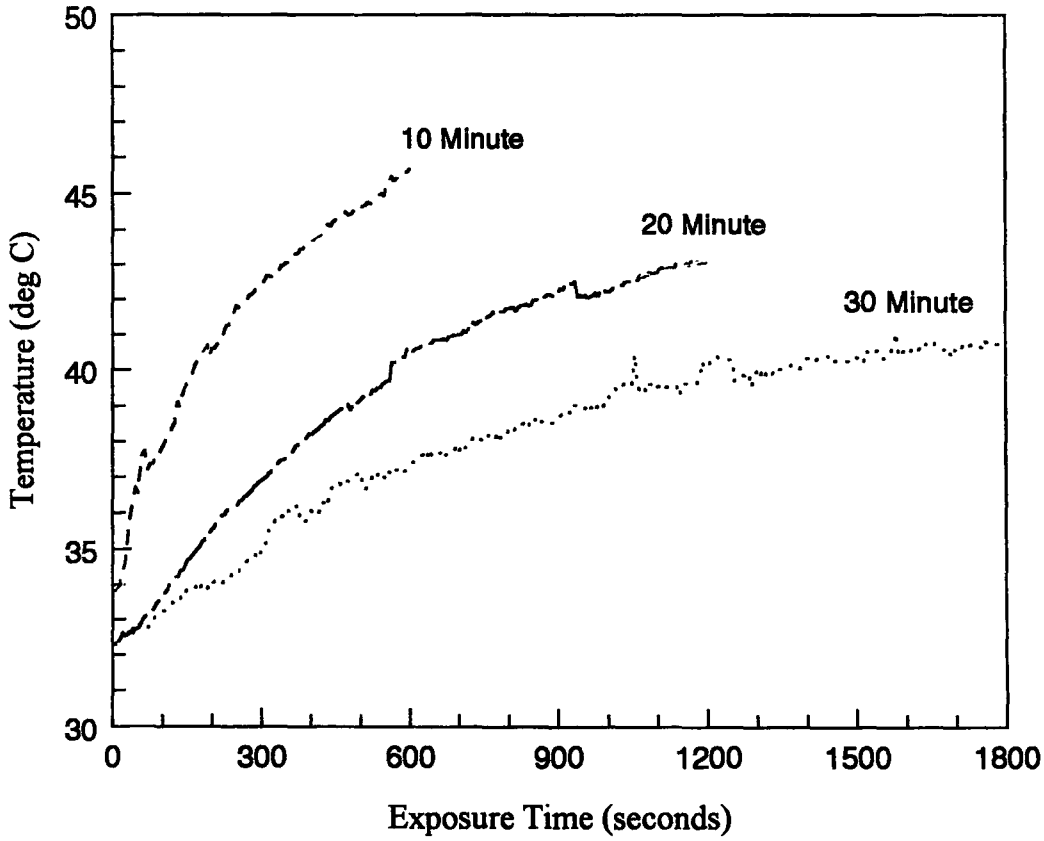

Figure 4.11: Experimental temperature response at the lesion boundary for each of a 10, 20, and 30 minute irradiation illustrating the higher temperatures required with shorter exposures to produce the same damage. Lesion producing temperatures were observed to be significantly lower than the 60°C generally associated with coagulation.

consistent with the correlation shown for other reported (E_a , α) pairs. Although the other reported values are also based on Arrhenius theory, they include experiments using a variety of different endpoints and tissue types, and generally use a constant temperature versus a transient response.

Finally, the lesion growth predicted by Arrhenius theory appeared to fit well to the experimental data. Using constant κ_{eff} and ρc values of 0.6×10^{-3} W/mm/K and 3 J/mm^3/K respectively, the theoretical curve passes through all three average radii corresponding to the three exposure groups within uncertainty.

4.5 SUMMARY

The temperature response and corresponding lesion production from *in vivo* interstitial laser photocoagulation were investigated in order to test the consistency of lesion growth predictions by Arrhenius theory. The theory is based upon the application of first order unimolecular rate kinetics to characterize thermal damage processes leading to different damage endpoints.

Irradiations were performed *in vivo* in rabbit muscle for various exposures at 1.0 W using an 805 nm diode laser source but with a pre-charred optical fibre tip, thereby forcing it to function as a point heat source. The delivery template consisted of an array of five microthermocouples positioned perpendicular to the optical fibre source and fixed to a thin Lucite annulus. This enabled accurate and reproducible measurements of the temperature response along a range of radial distances from the

point heat source. The lesions were resected 48 hours after irradiation, the necrosis boundary was determined histologically, and the lesion radius measured. The temperature-time history at the lesion boundary could then be interpolated after determining the precise radial position of the lesion boundary relative to the source and thermocouple array.

Numerical integration of the Arrhenius equation for the lesion boundary temperature profile was performed using the trapezoid rule. This was done for several activation energies, E_a, and the corresponding pre-exponential factor, α, was calculated for each E_a. The correlation between E_a and α for each set was found to be consistent with the correlation observed in other reported experimental values for varying thermal damage endpoints and tissue types.

The experimental temperature profiles from the five thermocouples for each of eleven irradiations were fit to the theoretical temperature distribution derived from the Weinbaum-Jiji bioheat transfer equation. The effective thermal conductivity, thermal diffusivity, and volumetric heat capacity were determined from the fit parameters. Both the thermal conductivity and volumetric heat capacity are generally assumed to be constant in solving the bioheat transfer equation. However, contrary to this, both were seen to vary inversely as a function of the radial distance from the source.

Finally, the theoretical lesion growth was determined by numerical integration of the Arrhenius integral for the theoretical temperature distribution and then iteratively solving for the lesion radius. The generated lesion radius curve as a

function of the exposure duration agreed well with the experimental lesion growth values.

APPENDIX A

```
; IDL (Interactive Data Language, ©Research Systems Inc., v. 3.5.1) program to
; numerically integrate the Arrhenius integral for transient temperature response.
; Temperature response used is the solution to the W-J bioheat transfer equation
; for a point heat source.
; Written by Tamie Poepping and Jeremy Gill, 1996.

FUNCTION TEMP_INTG, time      ;Temperature integrand, alpha*T*exp(-E/RT)

COMMON radius_block, r, Tamb, Ptotal, keff, rho, shc, rhoc, AE, mgc, alpha

     ;trtemp=transient temperature, T=Tamb + Ptotal/4(pi)(keff)r * erfc(r/Lth(t)

     ;temp_intg=integrand of Arrhenius integral, alpha*T*exp(-E/RT)

trtemp = Tamb + Ptotal/(4*!pi*keff*r) *(1- errorf(r/sqrt(4*keff*time/(rhoc))) )

return, alpha * trtemp * exp(-AE/ mgc/ double(trtemp) )

END


PRO INT_ARRH, OMEGA

;
; Program which integrates a function of the form
;   t
;  /
;  |
;  | T(t',r)F(t',r)dt'   (ie. T exp(-AE/RT) dt')
;  |
;  /
;  0
;

COMMON radius_block, r, Tamb, Ptotal, keff, rho, shc, rhoc, AE, mgc, alpha
```

```
Tamb=307          ;Ambient temp 307 K=34 C
Ptotal=1.0        ;Power delivered per unit volume, W/mm3
keff=6*1E-4       ;Effective thermal conductivity, W/mm/K

rho=1*1E-3        ;Density, g/mm^3
shc=3             ;Specific heat, J/g/K
rhoc=rho*shc      ;Volumetric heat cap., J/mm^3/K

AE=3E5            ;Activation energy, J/mol  (1E5 J/mol=100 kJ/mol)
mgc=8.314         ;Molar gas constant, 8.314 J/mol/K
alpha=1d44        ;Pre-exponential factor, s^-1, K^-1

; Define the range of relevant radii.

r_start = 0.2                              ;Define the starting radius
r_finish = 15.2                            ;Define the finishing radius
r_step = 0.2                               ;Define increment in radius
r_number = (r_finish-r_start) /r_step +1   ;Calc number of radius points

; Define range of exposure times for integration limits.

t = findgen(480)*5 + 5                     ;For t = 5-2400s by 5s.

; Define array that will hold results of integration.

OMEGA = fltarr( n_elements(t), r_number)   ;Omega(time,radius)
result = fltarr(r_number)

; For each value of radius, r, integrate function for
; times ranging from 0 to t.

FOR ir = 0, r_number-1 DO BEGIN
   print, ir
   r = r_start + ir * r_step               ;r=radius
   result = NR_QROMO("TEMP_INTG", 0, t)    ;Integrate fct TEMP_INT
                                           ;for exposure times
                                           ;over open interval (0,t)
                                           ;using Romberg integration.

   OMEGA(*,ir) = result                    ;Omega(time,radius)

ENDFOR
```

```
; Determine the coagulation/lesion radii, ie. the radii for which Omega~1.

  coag_indx = fltarr(n_elements(t))          ;r subscripts to Omega(t,r=rc).
  coag_rad = fltarr(n_elements(t))           ;Coagulation radii, coag_rad(time).

; For each possible exposure duration...
  FOR it = 0, n_elements(t)-1 DO BEGIN

     coag_indx(it) = max(where(OMEGA(it,*) ge 1.))
     coag_rad(it) = r_start + r_step * coag_indx(it)

        ;OMEGA(it,*) ge 1.   =>determine which elements satisfy Omega≥1
        ;                      ie Omega(t,r<rc)for each exposure time.
        ;where(    )         =>returns subscripts of above elements.
        ;max(      )         =>returns value of the largest subscript
        ;                      ie corr to largest r for which Omega≥1
        ;                      ie for r>rc, Omega is <1.
        ;coag_indx(it)       =>vector containing these subscripts.
        ;coag_rad(it)        =>vector containing coagulation radii.

    ENDFOR

  openw, 1, 'rcfile.dat
  printf, 1, format='(F)', coag_rad
  close, 1

END
```

BIBLIOGRAPHY

Agah R, Pearce JA, Welch AJ, and Motamedi M, 1994 "Rate process model for arterial tissue thermal damage: Implications on vessel photocoagulation" Lasers Surg. Med. 15:176-84.

Amin Z, Buonaccorsi G, Mills T, Harries S, Lees WR, and Bown SG, 1993 "Interstitial laser photocoagulation: Evaluation of a 1320 nm Nd-YAG and an 805 nm diode laser: the Significance of charring and the value of pre-charring the fibre tip" Lasers Med. Sci. 8:113-20.

Anvari B, Rastegar S, and Motamedi M, 1994 "Modeling of intraluminal heating of biological tissue: Implications for treatment of benign prostate hyperplasia" IEEE Trans. Biomed. Eng. 41(9):854-64.

Arkin H, Xu LX, and Holmes KR, 1994 "Recent developments in modeling heat transfer in blood perfused tissues" IEEE Trans. Biomed. Eng. 41(2):97-107.

Arrhenius, S, 1889 "Uber die reaktionsgeschwindigkeit bei der inversion von rohrwucker durch sauren" Z. f. Physik. Chemie IV:226-248.

Beacco CM, Mordon SR, and Brunetaud JM, 1994 "Development and experimental *in vivo* validation of mathematical modeling of laser coagulation" Lasers Surg. Med. 14:362-73.

Birngruber R, Hillenkamp F, and Gabel V-P, 1985 "Theoretical investigations of laser thermal retinal injury" Health Phys. 48:781-796.

Birngruber R, 1980 "Thermal modeling in biological tissues" in Lasers in Biology and Medicine, F. Hillenkamp, R. Pratesi, and C.A. Sacchi eds., New York: Plenum Press, 77-97.

Boulnois J, 1986 "Photophysical processes in recent medical laser developments: a Review" Lasers Med. Sci. 1:47-66.

Brinck H and Werner J, 1994 "Efficiency function: Improvemnt of classical bioheat approach" J. Appl. Physiol. 77(4):1617-22.

Calmettes P, Durand D, Desmadril M, Minard P, Receveur V, and Smith JC, 1994 "How random is a highly denatured protein?" Biophys. Chem. 53:105-14.

Carslaw HS and Jaeger JC, 1959 Conduction of Heat in Solids, 2nd ed., Oxford: Clarendon Press.

Charney CK, Weinbaum S, and Levin RL, 1990 "An evaluation of the Weinbaum-Jiji bioheat equation for normal and hyperthermic conditions" ASME J. Biomech. Eng. 112:80-87.

Cooper TE and Trezek GJ, 1971 "Correlation of thermal properties of some human tissue with water content" Aerospace Med. January:24-27.

Dowden J, Jordan T, and Kapadia P, 1988 "Temperature distribution produced by a cylindrical etched fibre tip in laser treatment of tumours by local hyperthermia" Lasers Med. Sci. 3:47-54.

Flotte TJ, Yashima Y, Watanabe S, McAuliffe D, and Jacques SL, 1990 "Morphological studies of laser-induced photoacoustic damage" SPIE (Laser-Tissue Interaction) 1202:71-77.

Frank F, 1989 "Laser light and tissue: Biophysical aspects of medical laser applications" SPIE (Lasers and Medicine) 1353:37-45.

Glenn TN, Rastegar S, and Jacques SL, 1996 "Finite element analysis fo tmeperature controlled coagulation in laser irradiated tissue" IEEE Trans. Biomed. Eng. 43(1):79-87.

Henriques FC and Moritz AR, 1947 "Studies of thermal injury II-V" Am. J. Pathol. 23

Hillenkamp F, 1980 "Interaction between laser radiation and biological systems" in Lasers in Biology and Medicine, F. Hillenkamp, R. Pratesi, and C.A. Sacchi eds., New York: Plenum, 37-68.

Hu CL and Barnes FS, 1970 "The thermal-chemical damage in biological material under laser irradiation" IEEE Trans. Biomed. Eng. BME-17(3):220-29.

Jacques SL and Prahl SA, 1987 "Modeling optical and thermal distributions in tissue during laser irradiation" Lasers Surg. Med. 6:494-503.

Jacques SL, Newman C, and He XY, 1991 "Thermal coagulation of tissues: Liver studies indicate a distribution of rate parameters, not a single rate parameter, describes the coagulation process" Proc. ASME Winter Annu. Meet. (Advances in Biological Heat and Mass Transfer) HTD-189/BED-18:71-73.

Johnson FH, Eyring H, and Stover BJ, 1974 The Theory of Rate Processes in Biology and Medicine New York:John Wiley & Sons.

Langerholc J, 1979 "Moving phase transitions in laser-irradiated biological tissue" Appl. Opt. 18:2286-93.

Law MP, 1988 "The response of normal tissues to hyperthermia" in Hyperthermia and Oncology Vol I, M. Urano and E. Douple eds., Utrecht: VSP, 121-59.

Malone DE, Wyman DR, Denardi FG, McGrath FP, De Gara CJ, and Wilson BC, 1994 "Hepatic interstitial laser photocoagulation: an Investigation of the relationship between acute thermal lesions and their sonographic images" Investigative Radiology 29(10):915-21.

Masters A, Steger AC, and Bown SG, 1991 "Role of interstitial therapy in the treatment of liver cancer" Br. J. Surg. 78:518-23.

Matthewson K, Coleridge-Smith P, O'Sullivan JP, Northfield TC, and Bown SG, 1987 "Biological effects of intrahepatic neodymium:yttrium-aluminum-garnet laser photocoagulation in rats" Gastroenterology 93:550-7.

McKenzie AL, 1990 "Physics of thermal processes in laser-tissue interaction" Phys. Med. Biol. 35(9):1175-1209.

Moseley H, 1994 "Ultraviolet and laser radiation safety (Review)" Phys. Med. Biol. 39:1765-99.

Muller GJ, Dorschel K, and Schaldach B, 1989 "Main problems and new results on dosimetry in laser medicine" SPIE (Lasers and Medicine) 1353:3-10.

Pearce JA, 1990 "Thermodynamic principles of laser-tissue interaction" Proc. Annual Int. Conf. IEEE Eng. Med. Biol., 12(3):1108-10.

Pearce JA and Thomsen S, 1995 "Rate process analysis of thermal damage" in Optical-Thermal Response of Laser-Irradiated Tissue, AJ Welch and MJC van Gemert eds., New York:Plenum Press, 561-606.

Pearce JA and Thomsen S, 1993 "Kinetic models of laser-tissue fusion processes" ISA 44:355-60.

Pennes HH, 1948 "Analysis of tissue and arterial temperatures in the resting human forearm" J. Appl. Physiol. 1:93.

Prapavat V, Roggan A, Walter J, Beuthan J, Klingbeil U, and Muller G, 1996 "In vitro studies and computer simulations to assess the use of a diode laser (850 nm) for laser-induced thermotherapy (LITT)" Lasers Surg. Med. 18:22-33.

Samulski TV, Lyons BE, and Britt RH, 1985 "Temperature measurements in high thermal gradients: II. Analysis of conduction effects" Int. J. Radiation Oncology Biol. Phys. 11:963-71.

Schrottner O, Ascher PW, and Ebner F, 1990 "Interstitial laser thermotherapy of brain tumors under MRI control" Fifth International Congress of the European Laser Association, Graz, Austria Abstract C-24:66.

Svaasand L, Boerslid T, and Oeveraasen M, 1985 "Thermal and optical properties of living tissue: Application to laser-induced hyperthermia" Lasers Surg. Med. 5:589-602.

Takata AN, Zaneveld L, and Richter W, 1977 "Laser-induced thermal damage in skin" USAF School Aerospace Medicine, Brooks AFB, TX, Rep. SAM-TR-77-38.

Takata AN, et al., 1974 "Thermal model of laser induced eye damage" USAF School of Aerospace Medicine, Brooks AFB, TX, Final Tech. Rep. IITRI, J-TR 74-6324.

Thomsen S, 1991 "Pathologic analysis of photothermal and photomechanical effects of laser-tissue interactions" Photochem. Photobiol. 53(6):825-35.

Thomsen S, Jacques S, and Flock S, 1990 "Microscopic correlates of macroscopic optical property changes during thermal coagulation of myocardium" SPIE (Laser-Tissue Interactions) 1202:2-11.

Thomsen S, 1995 "Identification of lethal thermal injury at the time of photothermal treatment" in Laser-Induced Interstitial Thermotherapy, G Muller and A Roggan eds., Bellingham:SPIE Publishers, 459-67.

Valvano JW and Chitsabesan B, 1987 "Thermal conductivity and diffusivity of arterial wall and atherosclerotic plaque" Lasers Life Sci. 1(3):219-29.

Vyas R and Rustgi ML, 1992 "Green's function solution to the tissue bioheat equation" Med. Phys. 19(5):1319-24.

Weaver JA and Stoll AM, 1969 "Mathematical model of skin exposed to thermal radiation" Aerospace Med. 40(1):24.

Weinbaum S and Jiji LM, 1985 "A new simplified bioheat equation for the effect of blood flow on local average tissue temperature" ASME J. Biomechanical Eng. 107:131-139.

Welch AJ, 1984 "The thermal response of laser irradiated tissue" IEEE J. Quantum Electron. QE-20(12):1471-81.

Welch AJ and Polhamus GD, "Measurement and prediction of thermal injury in the retina of Rhesus monkey" IEEE Trans. Biomed. Eng. BME-31:633-644 (1984).

Whelan WM and Wyman DR, 1995 "Investigations of large vessel cooling during interstitial laser heating" Med. Phys. 22(1):105-15.

Wilson BC, 1991 "Modelling and measurements of light propagation in tissue for diagnostic and therapeutic applications" in Laser Systems for Photobiology and Photomedicine, AN Chester et al. eds, New York: Plenum Press, 13-27.

Wyman DR, Whelan WM, and Wilson BC, 1992 "Interstitial laser photocoagulation: Nd:YAG 1064 nm optical fiber source compared to point heat source" Lasers Surg. Med. 12:659-64.

Wyman D, Wilson B, and Adams K, 1994 "Dependence of laser photocoagulation on interstitial delivery parameters" Lasers Surg. Med. 14:59-64.

Wyman DR and Whelan WM, 1994 "Basic optothermal diffusion theory for interstitial laser photocoagulation" Med. Phys. 21(11):1651-56.

Yang Y, Welch AJ, and Rylander HG III, 1991 "Rate process parameters of albumen" Lasers Surg. Med. 11:188-190.

Yoon G, Welch AJ, Motamedi M, and van Gemert MCJ, 1987 "Development and application of three-dimensional light distribution model for laser irradiated tissue" IEEE J. Quantum Electron. QE-23(10):1721-33.